Dalton Transactions

PAPER

Check for updates

How important is the coordinating atom in controlling magnetic anisotropy in uranium(III) single-ion magnets? A theoretical perspective†

Sourav Dey, [ID] Gunasekaran Velmurugan [ID] and Gopalan Rajaraman [ID] *

Theoretical investigation of actinide based nanomagnets is of paramount interest in the field of molecular magnetism as they offer remarkable properties compared to their lanthanide counterparts. Unlike lanthanides, the magnetic properties of actinides can be fine-tuned by modulating the ligand field as they possess a large metal–ligand covalency. In this regard, two complexes reported earlier have gained attention: $[U(BcMe)_3]$ (**1**) has been found to show Single-ion Magnet (SIM) characteristics whereas isomeric $[U(BpMe)_3]$ (**2**) does not exhibit any SIM behaviour. To unravel the origin of the differences observed in magnetic anisotropy, a detailed *ab initio* CASSCF study has been undertaken on the X-ray structure of complexes **1** and **2**. Since actinide compounds exhibit strong covalency, the desired active space needs to be benchmarked to address this issue. Here, we have enlarged the active space systematically from CAS (3,7) to CAS(3,12) where all 5f electrons in 5f orbitals are sequentially expanded to include five formally empty 6d orbitals. Our calculations reveal that the incorporation of the $6d_{z^2}$ orbital is vital in reproducing many experimental observables such as temperature dependent susceptibility, *g*-factors, ground state m_J level, and ground-state-excited-state gap. Inclusion of this orbital in the reference space is found to describe better the U···H−BH agostic interactions leading to significant variations in the computed parameters. Gaining from this understanding, we have carried out extensive bonding analysis within the DFT framework using tools such as Natural Bond Orbital (NBO) and Atoms In Molecule (AIM) to further probe these weak agostic interactions. Also, predictions to enhance the U-ligand covalency using U−sulphur bonds and the role of the U−C distance and C−U−C bite angles in the nature of anisotropy have been studied, and relevant magneto-structural correlations have been developed. Thus our results for the first time provide a comprehensive understanding of uranium based SMMs and offer ways to fine tune the anisotropy for experimental chemists.

Department of Chemistry, Indian Institute of Technology Bombay, Mumbai, 400076, India. E-mail: rajaraman@chem.iitb.ac.in
†Electronic supplementary information (ESI) available: Tables containing energies, structure analysis using SHAPE, orbital diagrams, relaxation mechanism developed, susceptibility comparison and AIM plots. See DOI: 10.1039/c9dt01869g
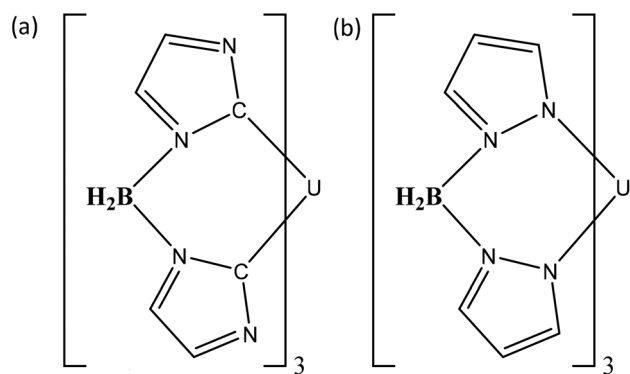
1. Introduction

Actinide single-ion magnets (SIMs) are gaining attention in the area of molecular magnetism, thanks to their covalency and multiconfigurational nature of the ground state rendering stronger anisotropy compared to 4f congeners. The renaissance in the field of molecular nanomagnets has begun after the discovery of slow magnetic relaxation on a double-decker complex $[TbPc_2]^-$ by Ishikawa *et al.* which exhibits a barrier height of 230 cm^{-1} for magnetisation reversal.[1] The strong spin–orbit coupling of lanthanides generates strong anisotropy which splits the ground state *J* manifold into $\pm m_J$ levels.[2] The suitable ligand field which minimises the electrostatic repulsion between the metal and ligand stabilises the spin–orbit coupled state with the highest m_J value. Due to weak covalency rendered by the lanthanides, the coordinating groups behave as electrostatic point charges and the variation of the coordinating groups only marginally influences the magnetic properties.[3]

On the other hand, the large covalency of actinides that can be compared to that of transition metals makes them a suitable candidate for SIMs.[4] They have the best of both worlds, combining the strong anisotropy like that found in lanthanides and tunable metal–ligand covalency that is attributed to transition metal complexes. These inherently enhance the exchange coupling constants of polymetallic SMMs.[4] Not only SMMs but also SIMs of actinides display better magnetic properties than lanthanides.[5] It has been found from the previous studies that the isoelectronic actinide complexes behave as

better SIMs compared to lanthanides due to their enhanced covalency.[5,6] The nature of the ground state can be modulated by varying the ligand field where the magnetic properties are strongly correlated with the symmetry of the molecule and the coordinating groups behave as a point charge which in a nutshell creates an electrostatic field.[7] The role of the coordinating atom controlling the anisotropy in a uranium(III) complex has been investigated by Long *et al.* in two trigonal prismatic isostructural complexes, [U(BcMe)$_3$] (**1**) and [U(BpMe)$_3$] (**2**) [BpMe]$^-$ = dihydrobis(methypyrazolyl)borate; [BcMe]$^-$ = dihydrobis(methylimidazolyl)borate (Fig. 1).[8] The complex with an N-heterocyclic carbene ligand displays a barrier height of magnetisation reversal (U_{eff}) of 33 cm^{-1} and this is one of the highest reported values to date for U(III) based SIMs, while [U(BpMe)$_3$] does not exhibit any signal in the ac measurement.[8] This unforeseen change of magnetic behaviour inspires us to study the two complexes to differentiate the origin of magnetic behaviour. Theoretical studies on actinide based SMMs are scarce due to the complexity involved in modelling such systems.[4] The complex electronic structure arises from the open shell 5f electrons and strong relativistic effects which makes the actinide chemistry very interesting. Due to the comparable energy of the 7p, 7s, 6d, and 5f orbitals, the ground state electronic structure is inherently multiconfigurational and to get a complete understanding of the electronic structure those orbitals need to be taken into consideration. Earlier studies on these systems suggest that 5f^3 states are sufficient to account for all energetically relevant Spin–Orbit (SO) effects while the susceptibility or *g*-factors are not accurately reproduced.[9]

Here *ab initio* CASSCF/PT2 calculations have been utilised to understand the nature of magnetic anisotropy in complexes **1** and **2**. The choice of the active space is crucial in *ab initio* studies of actinides, and therefore we have taken into consideration the 5f and 6d orbitals in our active space.[9] In our study, we have shown the role of 6d orbitals in agostic U···H interactions and their influence on the magnetic relaxation. The presence and absence of SIM behaviour in two complexes are rationalised using *ab initio* calculations. To understand the 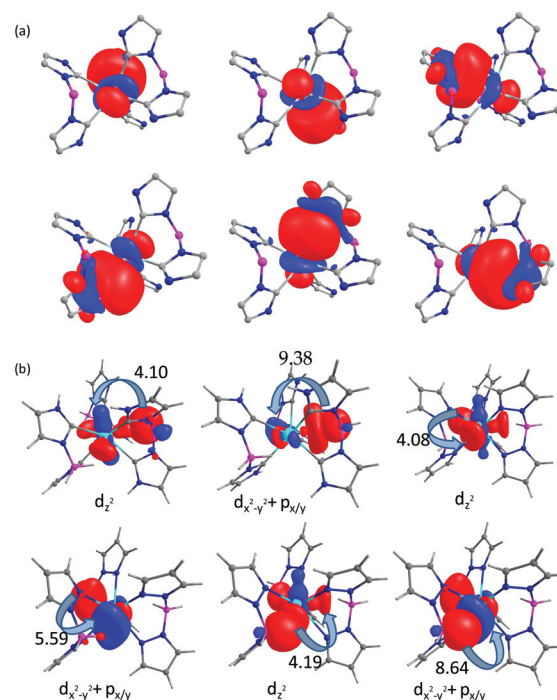nature of bonding and agostic interactions, we have also performed quantum theory of atoms in molecules (QTAIM) and natural bond orbital (NBO) analysis within the DFT framework.[10,11] Our study reveals that enhanced active space is vital to reproduce the experimental observables such as magnetic susceptibility and U_{eff} while smaller CAS reference space tends to overestimate the U_{eff} and the *g*-factors.[3,9]

2.   Computational details

All the *ab initio* multiconfigurational calculations have been carried out using the MOLCAS 8.0 programme package.[12] The spin free wave function was generated from the complete active space self-consistent field (CASSCF) level of theory.[13] To reduce the computational cost, all calculations were performed on models of complexes **1** and **2**, where the peripheral methyl groups on the imidazole ring were replaced by –H atoms on the X-ray structure (see Fig. 1 and 2). The all-electron atomic natural type with a relativistic core correction (ANO-RCC) basis set was employed for our calculations which address the large relativistic effect of uranium.[14] For complex **1**, the VTZP basis set for U and C atoms, the VDZP basis set for N and B atoms and the VDZ basis set for H atoms are employed. For complex **2**, as nitrogen atoms are coordinating to U, the VTZP basis set for N and the VDZP basis set for C atoms are used while maintaining the same basis set for other atoms as in complex **1**. In

Fig. 2 (a) NBO representation of uranium–carbon bonds in complex **1**. The isodensity surface shown corresponds to a value of 0.010 e$^-$ per bohr^3. (b) Second order perturbation theory donor–acceptor interaction along with their stabilization energy (kcal mol^{-1}) for donor σB–H to acceptor p–d hybrid orbital of U^{III} ions in complex **1** based on alpha spin orbitals. The isodensity surface shown corresponds to a value of 0.062 e$^-$ per bohr^3.

Fig. 1 (a) A schematic diagram of complexes (a) **1** and (b) **2**. Hydrogens are omitted for clarity.

the case of the model complex derived from **1**, the VTZP basis set was employed for U, C, N and S while VDZP and VDZ basis sets were employed for boron and hydrogen atoms, respectively. The relativistic effects were incorporated using Douglas–Kroll–Hess (DKH) Hamiltonian.[15] To reduce the size of the disk space, the Cholesky decomposition technique was employed.[16]

The employed active space has been divided into three categories, and this is summarised in Table 1. Methodology-I or MD-I consists of three electrons in seven 5f orbitals, *i.e.* CAS (3,7) while MD-Ia additionally includes three occupied 6p orbitals of uranium in RAS1 and three empty 6d orbitals in RAS3 space leading to RASSCF(9,13) notation. MD-II to VI were coined by the sequential inclusion of 6d orbitals of uranium along with 5f orbitals in the active space to account for 5f to 6d excitation (see Table 1).

MD-I and MD-Ia calculations were performed using 35 quartet and 112 doublet states. The quartet and doublet states of MD-II to MD-VI were optimized using all possible configuration state functions (CSFs). The 35 quartet and 112 doublet states were mixed using the RASSI-SO method to get the spin–orbit coupled states of uranium.[17] Increasing the number of roots in RASSI-SO was found to have no advantage, as the results obtained for MD-II to MD-VI using increased number of roots are invariant. We have also performed CASPT2 calculations with an IPEA shift of 0.25 on MD-I to gauge the role of dynamic correlation. To reduce the computational cost of CASPT2 calculations, here the number of quartet and doublet states was restricted to 35 and 40 CSFs, respectively.[18] Finally, magnetic susceptibility, *g* factors of the lowest doublets, blocking barrier and relaxation pathways were computed using the SINGLE_ANISO routine employing SO states obtained from the RASSI-SO procedure.[19–21]

Quantum theory of atoms in molecules (QTAIM) analysis was performed within the density functional theory framework using the hybrid B3LYP functional with a combination of effective core potential ECP60MWB[22] on uranium with its ECP60MWB_ANO basis set[23] and Alrichs TZV basis sets for all other atoms utilizing the Gaussian 09 suite.[10,24–28] QTAIM calculations were performed using the AIM2000 package.[29] Furthermore, employing the same setup, Natural Bond Orbital (NBO) analysis was performed using the Gaussian 09 suite.

Table 1 Summary of various active spaces employed in this work

Methodology (MD)	Orbitals employed	Notation
MD-I[a]	Seven 5f	CAS(3,7)
MD-Ia[a]	Seven 5f + three 6p + three 6d	RASSCF(9,13)
MD-II	Seven 5f + $6d_{z^2}$	CAS(3,8)
MD-III	Seven 5f + $6d_{z^2}$, $6d_{x^2-y^2}$	CAS(3,9)
MD-IV	Seven 5f + $6d_{z^2}$, $6d_{x^2-y^2}$, $6d_{xy}$	CAS(3,10)
MD-V	Seven 5f + $6d_{z^2}$, $6d_{x^2-y^2}$, $6d_{xy}$, $6d_{yz}$	CAS(3,11)
MD-VI	Seven 5f + $6d_{z^2}$, $6d_{x^2-y^2}$, $6d_{xy}$, $6d_{yz}$, $6d_{xz}$	CAS(3,12)

[a] Here 6p and 6d orbitals are included in RAS1 and RAS3 spaces, respectively.

Additionally, calculations have been performed to obtain the superhyperfine splitting of uranium nuclear spin in complex **2** using the B3LYP functional in the ORCA 4.0.1 programme package.[30] To reduce the computational cost, RIJCOSX approximation was used. The SARC-def2-TZVPP basis set was used for the uranium centre, the EPR-II basis set was used for nitrogen centres and the def2-TZVP basis set was used for all other atoms to calculate the hyperfine coupling constant. We have additionally performed *ab initio* ligand field calculations to obtain the orbital energy diagram of 5f and 6d orbitals using the ORCA 4.0.1 programme package.

3. Results and discussion

The X-ray structure of complexes **1** and **2** has idealised C_{3h} symmetry and possesses tricapped trigonal prismatic coordination geometry. The Continuous Shape Measures calculations (CShM) performed using SHAPE 2.1 software reveal that the deviation from the trigonal prismatic geometry is larger for **1** compared to **2** (see Tables S1 and S2†).[31] Additionally, complexes are found to have U⋯H–BH agostic interactions. The average U–C distance is found to be 2.662 Å while the U–N distance is found to be 2.588 Å. Consistently all the U–C bond distances are 0.1 Å longer. Additionally, the ligand bite angles are smaller by ∼3° for complex **1** compared to complex **2**. Here we set out to first explore the bonding in these two complexes using NBO and QTAIM analyses and explored the magnetic properties in the subsequent sections.

3.1. Probing the U-ligand bonding in complexes 1 and 2

To understand the intricate bonding details of complexes **1** and **2**, we have undertaken a detailed NBO and AIM analysis. Particularly the nature of the U–C bonding orbital and B–H⋯U agostic interactions are essential as these offer a clue on how such interactions can be utilised to control the magnetic anisotropy. The NBO analysis of U–C and U–N bonds implies that it is mainly formed by the s/p/d_{z^2} hybrid orbital of uranium (Fig. 2a, 3a and Tables S3 and S4†). The U–C bond is found to have ∼81% donation from C and ∼18% donation from U, while the U–N bond in complex **2** is found to have ∼90% contribution from N and ∼10% from U, reflecting a fact that U-ligand bonds are ionic in character in both complexes; however the U–C bonds in **1** have greater covalency than U–N in **2**. Therefore, the $6d_{z^2}$ orbital is playing an essential role in controlling magnetic anisotropy and reveals that this orbital might need to be considered for inclusion in the active space. Utilising the NBO donor–acceptor interaction derived from second-order perturbation theory, calculations reveal that larger stabilisation occurs from the methylimidazolyl borate ligand compared to the methylpyrazolyl borate ligand (Fig. 2b and 3b). This is due to the larger bite angle and the smaller U⋯H and U⋯B distance in **2** compared to **1**, which signifies the stronger agostic interactions in **2** compared to **1**.[8]

To further elucidate the nature of bonding and agostic interactions in **1** and **2**, we have performed topological analysis
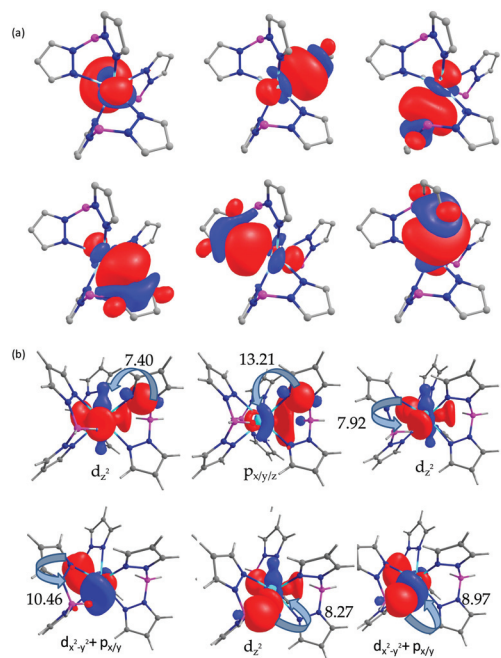
Fig. 3 (a) NBO orbitals of uranium–nitrogen bonds in complex **2**. The isodensity surface shown corresponds to a value of 0.010 e⁻ per bohr³. (b) Second order perturbation theory charge-transfer stabilization energy (kcal mol⁻¹) from donor σB–H to acceptor p–d hybrid orbital of U^III ions in complex **2** based on alpha spin orbitals. The isodensity surface shown corresponds to a value of 0.062 e⁻ per bohr³.

Table 2 Topological parameters at BCPs in the U–C(N) bonds. $\rho(r)$ in units of e Å⁻³, $G(r)$, $V(r)$, and $H(r)$ in units of a.u

Complex	$\rho(r)$	$\nabla^2_{\rho(r)}$	$H(r)$	ε	$|V(r)|/G(r)$
	U–C1(N1) bonds				
1	0.0505	0.0263	−0.0075	0.281	1.2196
2	0.0469	0.0385	−0.0020	0.330	1.0494
	U–C3(N3) bonds				
1	0.0504	0.0263	−0.0074	0.274	1.3089
2	0.0468	0.0381	−0.0019	0.314	1.0475
	U–C5(N5) bonds				
1	0.0505	0.0267	−0.0074	0.288	1.2170
2	0.0469	0.0381	−0.0019	0.304	1.0474
	U–C2(N2) bonds				
1	0.0498	0.0280	−0.0068	0.278	1.1954
2	0.0480	0.0379	−0.0024	0.331	1.0595
	U–C4(N4) bonds				
1	0.0497	0.0281	−0.0067	0.265	1.1954
2	0.0480	0.0375	−0.0024	0.313	1.0602
	U–C6(N6) bonds				
1	0.0498	0.0287	−0.0067	0.285	1.1887
2	0.0481	0.0376	−0.0024	0.309	1.0625
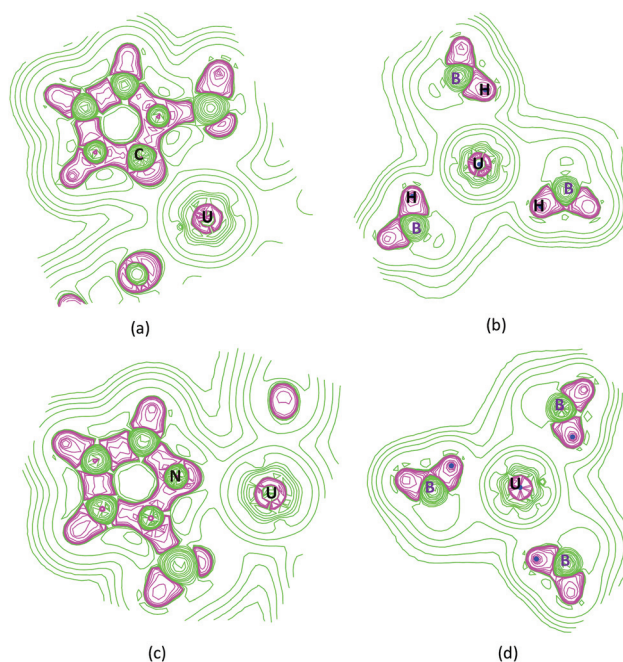
Fig. 4 Contour line diagram of the Laplacian of electron density (a) complex **1** along the U–C plane, (b) complex **1** along the U⋯H–BH plane, (c) complex **2** along the U–N plane and (d) complex **2** along the U⋯H–BH plane. Solid green lines indicate charge depletion [$\nabla^2_{\rho(r)} > 0$] and solid red lines indicate charge concentration [$\nabla^2_{\rho(r)} < 0$].

based on AIM (see Computational details for more explanation). The bonded and the non-bonded interactions present in the complexes **1** and **2** are confirmed with the presence of bond-critical points (BCPs). The big circles in the molecular graph indicate the atom positions. The critical points such as (3, −1), (3, +1) and (3, +3) correspond to bond (red), ring (yellow) and cage(green) critical points, respectively (Fig. S1†). The uranium centre has six bonds with each ligand *via* C/N atoms and it has two different bond paths which include six U⋯C(N) type and three U⋯H–B type interactions (see Fig. S1 in the ESI†). At the BCP between U and C/N atoms, the electron density $\rho(r)$ is found to be small (0.0469 a.u. < $\rho(r)$ < 0.0405 a.u.) and $\nabla^2_{\rho(r)}$ values are small and positive (0.0263 a.u. < $\nabla^2_{\rho(r)}$ < 0.0385 a.u.) (Table 2). This indicates a "closed" shell character of coordination bonds.

The $|V(r)|/G(r)$ ratio of the topological properties at U–C/N BCPs indicates a mixed character of coordination bonds with respect to the $|V(r)|/G(r)$ values (1.0595–1.1954 au) (Table 2). The small negative values of the total energy density $H(r)$ also support these findings. The electron density $\rho(r)$ values of complex **1** are higher than those of complex **2**, suggesting a stronger interaction present in **1**. The valence shell charge concentration (VSCC) zone of the carbenic carbon atom is more diffused (see Fig. 4a and c) towards the uranium (complex **1**) than the pyrazole nitrogen atom (complex **2**). This indicates that there is a substantial charge transfer from the carbenic carbon atoms to the uranium. The $\rho(r)$ values at the U⋯H–B

BCPs show 0.0146–0.0196 a.u., indicating very weak interaction between the uranium and H–B units (Table 3). This smaller $\rho(r)$ and positive $\nabla^2_{\rho(r)}$ value at the BCPs (U⋯H–BH) shows closed-shell interactions of agostic type. The positive total energy density $H(r)$ also suggests a very weak interaction. In addition, the $|V(r)|/G(r)$ values at the U⋯H–B BCPs yield a value less than 1 a.u. (0.8739–0.9262 a.u.) indicating ionic U⋯H–B interactions. It is interesting to note that bond paths between the uranium and H–B are characterized as the agostic

Table 3 Topological parameters at BCPs in the U···H–BH bonds. $\rho(r)$ in units of e Å^{-3}, $G(r)$, $V(r)$, and $H(r)$ in units of a.u

Complexes	$\rho(r)$	$\nabla^2_{\rho(r)}$	$H(r)$	ε	$|V(r)|/|G(r)|$
	U···H1–BH				
1	0.0196	0.0159	0.0011	0.9516	0.9262
2	0.0146	0.0125	0.0014	0.6754	0.8829
	U···H2–BH				
1	0.0196	0.0159	0.0011	0.9486	0.9257
2	0.0146	0.0125	0.0014	0.6753	0.8739
	U···H3–BH				
1	0.0197	0.0160	0.0011	0.9485	0.9262
2	0.0147	0.0125	0.0014	0.6705	0.8750

type which is confirmed by the straight bond paths at the uranium centre and highly curved at the agostic hydrogen (see Fig. S1†). The higher ellipticity (ε) values at the U···H–B BCPs also confirm the presence of U···H–B agostic interactions. The distance between the BCPs and agostic hydrogen atoms is too small, whereas the distance between the BCPs and uranium is larger. All these findings agree well with the earlier[32–34] reports. The Laplacian of electron density drawn along the U···H–BH plane clearly shows the presence of agostic interactions (Fig. 4b and d).

To gain insight into metal–ligand bonding, we have analysed the Mulliken charges and spin densities from the DFT calculations. In both the complexes, positive spin density is found on the uranium, and a small negative spin density is found at the ligand centres attached to uranium (Fig. 5). It signifies a mixture of spin polarisation and spin delocalisation although spin polarisation is dominant. Mulliken charge analysis reveals that strong crystal field is originating from the methyl imidazolyl borate ligand as the sizeable negative charge is found on the nitrogen atoms attached to the metal in **2** compared to the negative charges found on the carbon atoms attached to the uranium in **1** (see Table S5†). This suggests that the U-ligand bonds in complex **1** are more covalent compared to U-ligand bonds in complex **2**.

## 3.2 Mechanism of magnetization relaxation in 1 and 2

The energies of all the quartet and doublet states computed using MD-I are shown in Fig. S2 in the ESI.† The energies of
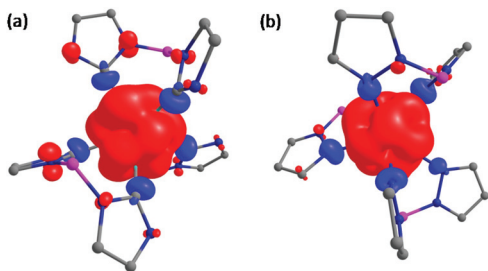

Fig. 5 DFT computed spin density plot of complexes (a) **1** and (b) **2**. The red and dark blue surfaces correspond to the positive and negative spin densities respectively. The isodensity surface shown corresponds to a value of 0.002 e^{-} per bohr^3.

the Kramers doublets (KDs) generated from the $^4I_{9/2}$ spin–orbit coupled state span up to 448 and 541 cm^{-1} for **1** and **2**, respectively (see Tables S6 and S7 in the ESI†). Due to the difference in the nature of the donor atoms and the accompanied structural differences, complex **2** has larger energy splitting compared to complex **1**.[8] The computed g_z axis of both complexes is oriented along the C_3 axis (see Fig. 6), in line with the expectation.

We would like to describe general mechanistic pathways of magnetisation relaxation expected for lanthanide/actinide complexes. In the absence of intermolecular interactions,
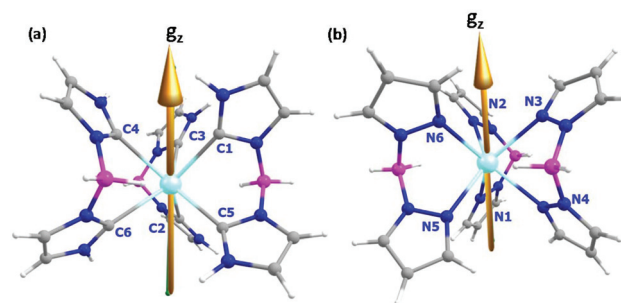
Fig. 6 Structure of complexes (a) **1** and (b) **2** along with the computed g_z axis. Colour code: U – cyan, N – blue, C – grey, B – pink and H – white.
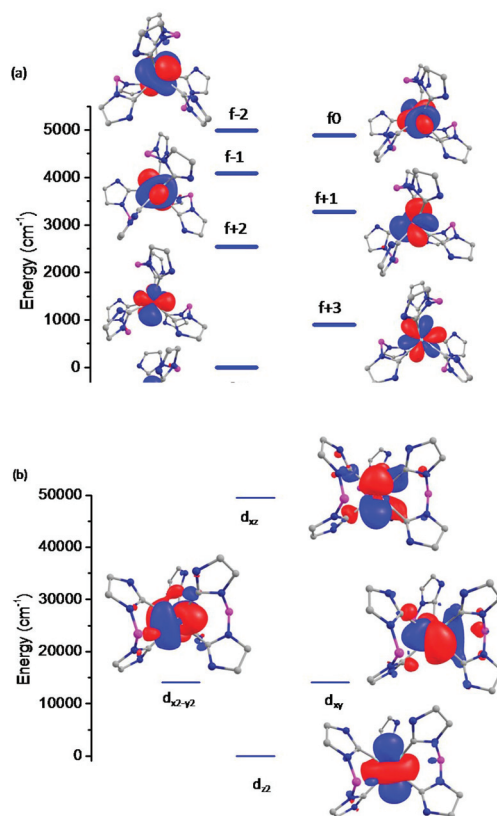
Fig. 7 Energy level diagrams of (a) 5f and (b) 6d orbitals in **1**. Colour code: U – cyan, N – blue, C – grey, B – pink. H-Atoms are removed for clarity.

relaxation is likely to occur *via* direct, Raman, Orbach and Quantum Tunnelling of Magnetisation (QTM) processes.[7] A large transverse anisotropy generally facilitates QTM in the ground state Kramers doublet. While this offers a primary path for QTM, other effects such as hyperfine splitting of U and coordinating atoms could further facilitate this process.[4] This is a pure tunnelling regime and is expected to be a temperature independent phenomenon. Also, the relaxation process includes magnetisation tunnelling *via* excited state(s) called thermally assisted QTM (TA-QTM) process and this is a temperature dependent phenomenon.[4] In the case of the direct process, the relaxation occurs *via* the emission of single phonon energy which matches with the difference in energy between the electronic states. The non-coincidence of the anisotropy axes of the excited KDs with the ground KD forces it to relax leading to the Raman/Orbach process.[35] Furthermore, the Raman process is of two types: first and second-order Raman processes. In the first-order Raman process, the energy released by the relaxation of spin by a molecule is absorbed by the superposition of two lattice waves whose frequency differences match those of the released energy.[3,36] This a two-phonon process involving a lattice state commonly called a virtual intermediate state. In the second order Raman process, not only the two lattice phonons but also the molecule goes through the virtual intermediate state to relax to the ground state.[7] If one magnetic system absorbs one phonon which excites

it to a higher energy state and then it relaxes *via* emission of phonons by interacting with the lattice this is called Orbach process, and this process is observed in many lanthanide SIMs.[36]

The computed *g*-anisotropy of the ground state Kramers doublet (KD1) of both complexes reveals an axial set of *g*-factors with strong transverse terms. While the calculated *g* factors and magnetic susceptibility (see Fig. 8 and Table 4) are in agreement with the experimental estimates for **2**, the values are overestimated for **1**. The relaxation mechanism of both complexes is similar except for the larger KD2–KD1 gap (here KD2 denoted the first excited Kramers doublet) for **2** compared to **1** (Fig. 9). The KD1 is dominated by the $m_J = |\pm 7/2\rangle$ state generated from the $^4I_{9/2}$ multiplet and this state mixes strongly with other m_J states giving rise to a substantial QTM prob-

Table 4 *Ab initio* computed *g* factors of complexes **1** and **2** using MD-I

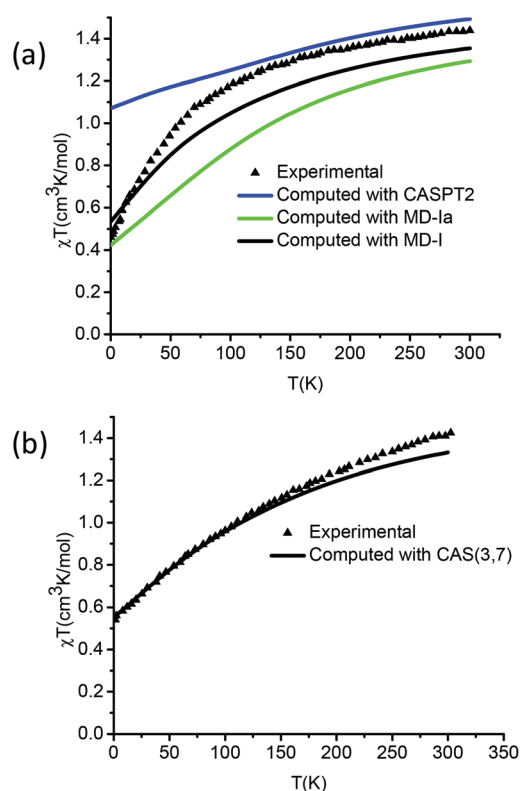|		g_x	g_y	g_z
1	Computed	2.58	2.53	2.00
	Experiment	2.57	2.57	1.03
2	Computed	2.63	2.61	1.97
	Experiment	2.62	2.62	1.76

Fig. 8 (a) Computed magnetic susceptibility data of complex **1** with different methodologies employed, see Table 1. (b) Computed magnetic susceptibility in comparison with the experiment of complex **2** using the CAS(3,7) setup.
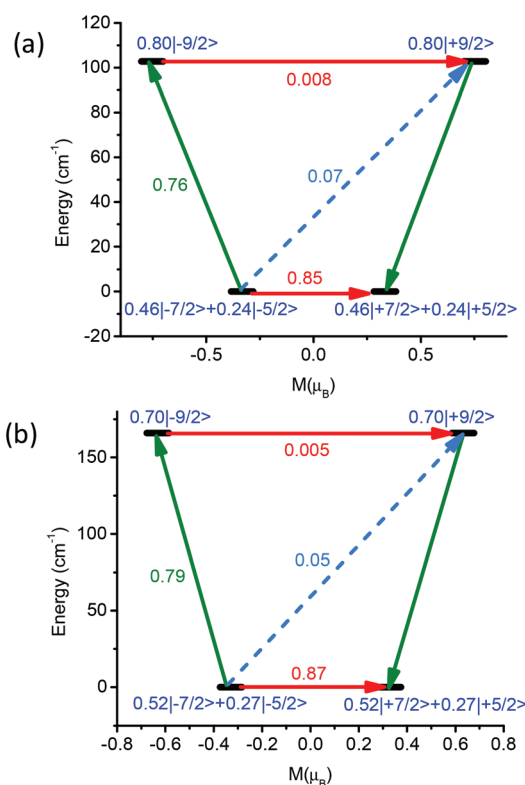
Fig. 9 (a) Qualitative mechanism of magnetic relaxation pathways computed for complex **1** and (b) **2**. The black line indicates the KDs as a function of magnetic moments. The red line represents QTM *via* ground states and TA-OTM *via* excited states. The dashed sky blue line indicates a possible Orbach process. The olive line indicates possible pathways of magnetic relaxation. The blue characters show the m_J composition of the KDs derived from the $^4I_{9/2}$ ground state.

ability ($0.85\mu_B$) (Fig. 9). The computed anisotropy of the first excited Kramers doublet (KD2) is approaching a pure $m_J = |\pm9/2\rangle$ state with a small mixing of other states leading to a diminished TA-QTM probability. It is worth noting that the QTM, TA-QTM probabilities and the coefficients of Orbach process remain similar for both the complexes (Fig. 9). While these results are in agreement with the absence of SIM behaviour observed in experiments for complex **2**, they are in contrast to the experimental observation of out-of-phase ac signals with an applied magnetic field for complex **1**. Clearly, the smaller reference space (MD-I) used has not captured all the metal–ligand covalency and therefore demands an expansion of reference space to correlate the mechanism with experimental observations. The computed blocking barrier of uranium-based complexes obtained from *ab initio* calculations is often overestimated compared to experimental U_{eff} values.[9,37] While there are various reasons for this discrepancy, it is important to note here that the blocking temperature computed for uranium SIMs considers Orbach as the dominant relaxation mechanism, while in reality magnetisation relaxes *via* the Raman/other process leading to a smaller barrier height than that computed.[9,38]

While the computed QTM reflects only about the anisotropy of the U(III) centre, additional flexibility such as hyperfine (not applicable here for U(III) with natural isotopes) and super-hyperfine splitting may further facilitate the QTM. In this respect, complex **2** with six nitrogen atoms coordinated to the uranium centre has a nuclear spin of $I = 1$ and is therefore expected to enhance the QTM compared to complex **1** where coordinated carbon atoms have no nuclear spins (for the abundant isotopes). The extent of the QTMs is correlated with the strength of hyperfine splitting and to gain further understanding of these issues, we have computed the super-hyperfine splitting of ^{14}N atoms in complex **2** using ORCA. The computed super-hyperfine values are shown in Table 5. The values are found to be small suggesting a very little delocalisation of spin densities on the nitrogen atom (see Table 5 and Fig. 2). However, the splitting is sufficient to facilitate further QTM even in the presence of applied field conditions. This suggests that the QTM in complex **2** is expected to be larger than that in **1** and rationalise the absence and presence of SIM behaviour in these complexes, respectively.

Further expansion of the reference space was undertaken using the MD-Ia setup (see MD-Ia in computational details

and Fig. S3 in the ESI† for orbital pictures). The three 6p and three 6d orbitals are found to be localised on the uranium centre with a minimal mixing with ligand MOs (Fig. S3;† the occupation of bonding orbitals becomes 1.98 and their corresponding unoccupied orbitals are 0.01). Inclusion of these six orbitals leads to enhancement of the crystal field splitting of all levels; in particular the energy gap between the KD1 and KD2 was increased (Table S8†). However, no improvements in other quantifiable properties such as *g* factors of the KD1, magnetic susceptibility data, *etc.* were observed. It suggests that this choice of reference space expansion is perhaps not ideal, as it does not capture greater metal–ligand covalency better than the earlier setup.

We have performed CASPT2 calculations on **1** where the dynamic correlation was taken into account using second-order perturbation theory. The CASPT2 results are summarized in Table 6 and Table S9 in the ESI.† The computed susceptibility data from CASPT2 are more inferior compared to the CASSCF results (Fig. 8), while this could be attributed to insufficient reference space/roots, this is a general trend in actinide chemistry as has also been noticed by other groups.[7,9,37,39–43] The CASPT2 calculations also reduce the QTM to $0.02\mu_B$ which suggests that complex **1** can behave as a zero-field SIM. However, the blocking barrier estimated is 141 cm^{-1}, and this is significantly larger when compared to the experimental value of 33 cm^{-1} (Fig. S4 in the ESI†). Thus our calculations also reiterate the fact that the CASSCF calculations with extended reference space are perhaps sufficient for the actinides.

To gain a more in-depth insight into the relaxation mechanism, we have analysed the computed crystal field parameters (we have used isoelectronic Nd(III) for computing crystal field parameters) which are expressed by crystal field Hamiltonian $\hat{H}_{CF} = \sum\limits_{k}\sum\limits_{q=-q}^{q} B_k^q \tilde{O}_k^q$ as implemented in SINGLE_ANISO where B_k^q is the crystal field parameter and $\tilde{O}_k^q$ is the Steven's operator.[12] The axiality of the complex increases the axial crystal field parameters and reduces the non-axial crystal field parameter. The computed axial field parameter ($k = 0$, $q = 2$) is larger than non-axial crystal field parameters ($k = 0$, $q \neq 2$) which supports the SIM behavior of complex **1** (see Table S10 in the ESI†).

Roles of formally empty 5d orbitals in dictating the sign and magnitude of magnetic coupling in 4f–4f and 3d–4f pairs are well addressed earlier by us and others.[44–48] Although the

Table 5 Computed super-hyperfine coupling constants of nitrogen atoms coordinated to U in **2**. All the values are given in cm^{-1} (see Fig. 2 for atom labels)

	A_x	A_y	A_z	$A(\text{iso})$
N1	-3.45×10^{-5}	-5.82×10^{-5}	-6.01×10^{-5}	-5.10×10^{-5}
N2	-9.11×10^{-6}	-3.78×10^{-5}	-4.29×10^{-5}	-2.99×10^{-5}
N3	2.97×10^{-5}	3.48×10^{-5}	7.77×10^{-5}	4.74×10^{-5}
N4	-6.46×10^{-5}	-8.23×10^{-5}	-8.61×10^{-5}	-7.77×10^{-5}
N5	-5.58×10^{-5}	-7.51×10^{-5}	-7.79×10^{-5}	-6.96×10^{-5}
N6	-4.90×10^{-6}	-8.31×10^{-6}	2.91×10^{-5}	5.34×10^{-6}

Table 6 Computed energy of the KDs (cm^{-1}) using different active space employed along with CASPT2 results for complex **1**

Complex **1**	MD-I	MD-Ia	CASPT2
KD1	0.00	0.00	0.00
KD2	102.7	220.1	141.9
KD3	318.5	306.6	295.3
KD4	409.9	548.9	339.9
KD5	448.1	708.7	499.3

magnetic anisotropy of lanthanides is strongly influenced by the incorporation of 5d orbitals into the active space, the scenario in actinides is very different.[49] To elucidate more in-depth insight into the role of the 6d orbital in the active space and why these orbitals influence the magnetic anisotropy strongly, we have analysed the nature of these 6d orbitals. The ligand bite angle of **1** is shorter by 3° than **2** which increases the U⋯H–BH distance in **1**.[8] The role of weak Ln⋯OH$_2$ interactions in influencing the magnetic anisotropy is well established.[50,51] Earlier by studying in detail the bonding in lanthanide analogues of complexes **1** and **2**, we have established the importance of M⋯H agostic interactions in controlling the magnetic anisotropy.[32] Due to the greater availability of 5f orbitals compared to 4f, the agostic interactions are expected to be stronger in the actinides. Interestingly, a closer look at the 6d orbitals that are included in the reference space reveals that these orbitals have small but non-negligible B–H bond contributions and hence help depict agostic interactions in the multiconfigurational methods (Fig. 2 and 3). Formally agostic interaction represents donation of C–H bond electrons into the coordinatively unsaturated orbitals of transition metals. Here the donations are expected for the frontier 6d orbitals of the metals and hence this important bonding feature is partly captured in our calculations. Additionally, since 6d and 5f orbitals of U(III) lie very close in energy, the inclusion of 6d orbitals offers further flexibility.

3.3. Assessing the role of 6d orbitals of U in reproducing the susceptibility data

In this section, the active space has been extended to include 6d orbitals to assess their role in influencing the magnetic properties of these two complexes. To begin with, we have included the $6d_{z^2}$ orbital (MD-II) in the active space. The $6d_{z^2}$ orbital was found to be the lowest lying in energy among all the 6d orbitals (Fig. 7). The energy gap between the KD1 and KD2 as well as the overall crystal field splitting of the $^4I_{9/2}$ state is found to be smaller with the MD-II setup (Table 7). The computed magnetic susceptibility data match very well with experimental data – a rare example in U(III) chemistry (Fig. 10).

The g_x, g_y, and g_z values also match well with the experimental ones (Table 7). Calculations reveal that the magnetic ground state consists of $m_J = |{\pm}5/2\rangle$ and $|{\pm}7/2\rangle$ states which are in line with the experiments (Table S11†). Therefore, the addition of the $6d_{z^2}$ orbital has improved the computed results demonstrating the need to include this orbital in the reference space. The addition of the $6d_{z^2}$ orbital in complex **2** improves the computed magnetic susceptibility and g-factors compared to experiments (Table S12 and Fig. S5 in the ESI†). Very recently a trigonal prismatic U(III) complex has been reported where a pivotal role of $6d_{z^2}$ in dictating the bonding has been highlighted. As the geometries of complexes **1** and **2** are also trigonal prismatic where the energy of the $6d_{z^2}$ orbital is expected to be lower compared to the other 6d orbitals (see Fig. 3), the inclusion of this orbital is vital in reproducing all the experimental observables in complexes **1** and **2**.

Table 7 Computed energy spectrum along with g factors of the uranium centre using MD-II–MD-VI in the complex in **1**

| States	MD-II				MD-III				MD-IV				MD-V				MD-VI			
	E	g_x	g_y	g_z	E	g_x	g_y	g_z	E	g_x	g_y	g_z	E	g_x	g_y	g_z	E	g_x	g_y	g_z
KD1	0.00	2.735	2.667	1.596	0.0	2.027	2.169	3.013	0.0	0.069	0.090	5.069	0.0	0.799	2.109	3.650	0.0	0.007	0.040	5.057
KD2	84.1	0.025	0.033	3.735	90.4	0.130	0.746	4.696	36.5	2.617	2.490	1.225	21.5	0.494	1.313	3.656	40.7	1.021	1.077	3.025
KD3	218.9	3.311	3.247	0.502	279.3	3.159	2.087	0.866	209.9	2.936	2.844	0.400	265.0	0.071	0.996	3.185	127.5	0.986	1.231	4.076
KD4	292.7	3.349	2.493	0.043	356.8	0.402	0.951	2.888	251.1	0.090	0.460	1.668	335.2	0.812	1.298	4.169	144.6	0.094	0.352	2.187
KD5	297.7	0.895	0.641	0.061	373.7	0.357	1.815	4.639	258.0	3.161	2.247	0.427	413.1	0.137	0.551	5.022	238.3	3.373	2.925	0.701
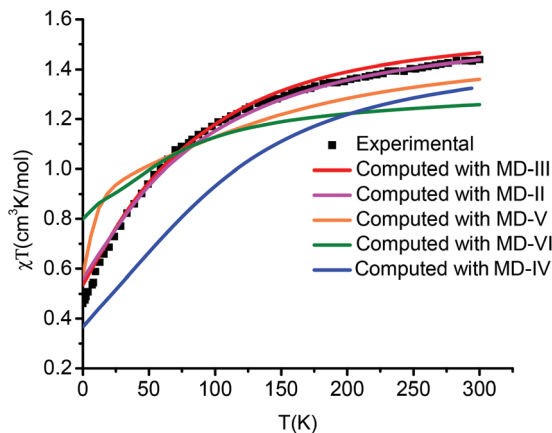
Fig. 10 Comparison of magnetic susceptibility computed using various methodologies for complex **1** (see Table 1 for further details).

In the next step, we have included another 6d orbital (MD-III) and repeated the calculations. Using this setup, the computed magnetic susceptibility is found to match well with experiments; however, the computed g_x and g_y values are underestimated and the g_z value is overestimated compared to the experimental results. The overall energy splitting of the KDs increases to 80 cm^{-1} compared to that of the MD-II (Table 7). The QTM probability computed at the ground state becomes larger and this is essentially due to the enhancement of the transverse anisotropy upon addition of one more 6d orbital into the reference space. The energy gap KD1–KD2 is 90 cm^{-1} and this is three times higher than the estimated experimental U_{eff} value (33 cm^{-1}). The ground KD is mainly composed of $m_J = |\pm 7/2\rangle$ along with a minor contribution from other states (Table S11†).

In the MD-IV set up, the energy gap between KD1 and KD2 has been reduced to 36 cm^{-1} and this is accompanied by a small transverse anisotropy in the KD1 (Table 7). However, the magnetic susceptibility and g factors computed using this set up do not match with experimental values (Fig. 10 and Table 7).

In the MD-V set up, the KD1–KD2 energy gap decreases to 21 cm^{-1}, which is very close to the experimental value; however the overall crystal field splitting of the $^4I_{9/2}$ state increases (Table 7). The computed g_x and g_y values are underestimated and the g_z value is overestimated compared to experimental values. The ground state QTM probability decreases and this signifies that complex **1** has the potential to behave like a zero-field SIM. The ground state wave function has a significant contribution from the $m_J = |\pm 9/2\rangle$ state (Table S11†). Therefore, adding this extra 6d orbital which lies very high in energy in the reference space leads to no significant improvement in the magnetic properties.

In the end, we have expanded the reference space to CAS (3,12) (MD-VI). The inclusion of all the 6d orbitals in the active space decreases the overall energy splitting of the KDs as well as the KD1–KD2 energy gap (Table 7). The QTM also diminishes, and the computed magnetic susceptibility shows a significant deviation in the lower temperature region com-

pared to the experiments. The ground state g_x and g_y values are underestimated, and the g_z value is overestimated. The KD1 mainly consists of the $m_J = |\pm 9/2\rangle$ state, and this is purely Ising in nature, and this is also in contrast to the EPR data obtained from the experiments (Table S11†).

Significant donor–acceptor interactions found in the NBO second-order perturbation theory analysis reveal that d_{z^2}, $d_{x^2-y^2}$ and $p_{x/y}$ orbitals of uranium interact strongly with –BH$_2$ protons to stabilise the complex (Fig. 2b and 3b). We have shown (see Fig. 7) the energy splitting diagram of 6d orbitals in the trigonal prismatic environment. The inclusion of the $6d_{z^2}$ orbital in the active space leads to additional flexibility and internal electron transfer from 5f to 6d orbitals. Another study by Zhu *et al.* also ascertains this finding in which authors have claimed that uranium(III) ions in a trigonal prismatic environment achieve a $5f^2 6d^1$ configuration. In this configuration, the valence MOs are found to have substantial contributions from the $6d_{z^2}$ orbital than other 6d orbitals.[52] Additionally, the incorporation of the $6d_{z^2}$ orbital *via* the CAS(3,8) active space partially takes into account the agostic interactions which decrease the energy splitting of the KDs and improves the agreement with experiments on the quantifiable parameters such as magnetic susceptibility and g factors.

The computed magnetic susceptibility using the MD-III set up is also found to offer good agreement with various experimental quantities including an excellent match to the experimental susceptibility data. As the $6d_{x^2-y^2}$ orbital is strongly destabilised compared to the $6d_{z^2}$ orbital, its inclusion seems to enhance the g_z value leading to a significant overestimation of the g-factors. The addition of higher energy $6d_{xy}$, $6d_{xz}$ and $6d_{yz}$ orbitals which are π^* in character leads to a stronger donation from the π cloud of the ligands and hence overestimates the KD splittings. To balance these effects, one has to include the corresponding ligand bonding π orbitals but this would increase the CAS reference space significantly as there are multiple close lying ligand π orbitals.

3.4. Increasing the U_{eff} value by *in silico* design

As stated earlier, the primary motive in the area of SIMs is to increase the barrier height for magnetisation reversal. Larger U_{eff} values may offer attractive blocking temperatures desired for the potential applications proposed. Studies on complexes **1** and **2** reveal that significant U-ligand interaction is the key to increase the barrier height. Keeping this in mind, here we attempt to model *in silico*, a new ligand containing sulphur donors which could possibly enhance the U-ligand covalency and hence U_{eff} values. Thus here, we have modelled a ligand where the carbon donor atoms are replaced by sulphur atoms in complex **1**. The molecular structure along with the computed g_z anisotropy of this model is shown in Fig. 11. The U–S and N–S bond lengths have been fixed from the literature values for similar structures.[53–56] Calculations performed using the MD-I setup reveal that the g_z value is 0.352 for the KD1 and this is very small compared to the same in complexes **1** and **2**. The axiality of the complex is found to be larger than
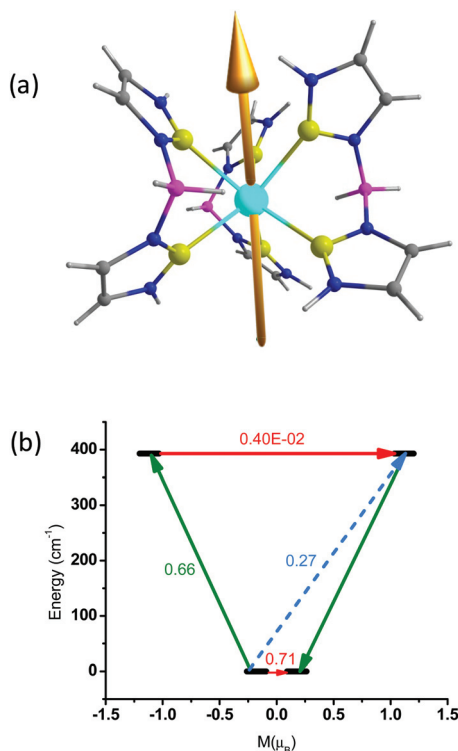
Fig. 11 Anisotropy axis of the model complex (up). Mechanism of relaxation pathways (down). The black line indicates the KDs as a function of magnetic moments. The red line represents QTM *via* ground states and TA-OTM *via* excited states. The dashed line indicates a possible Orbach process. The olive line indicates possible pathways of magnetic relaxation. Colour code: U – cyan, S – yellow, N – blue, C – grey, B – pink.

that of **1** and **2**, and the anisotropy axis is found to be oriented along the C_3 axis. Since the MD-II reproduces the experimental observables for **1**, this methodology has been applied to this model complex (see Table S13 in the ESI†). The energy splitting of the KDs is found to increase with this methodology.

The ground state QTM diminishes compared to that for other two complexes, and the energy splitting of the KDs is found to reach a value of 1376 cm^{-1} signifying the importance of U–S bonds in enhancing the overall crystal field splitting compared to complexes **1** and **2** (Table 8). The nature of the magnetic relaxation pathways, however, remains similar to complexes **1** and **2** with TA-QTM probability of the first excited state found to be smaller than the QTM.

Table 8 Computed energy splitting along with g factors of the uranium centre in model complex using MD-I

	Energy (cm^{-1})	g_x	g_y	g_z
KD1	0.0	2.141	2.122	0.352
KD2	392.8	0.002	0.017	2.236
KD3	1176.4	2.691	2.667	0.582
KD4	1271.5	0.034	0.047	2.597
KD5	1376.3	2.412	2.358	0.923

3.5. Magneto-structural correlations

To get a better understanding of the dependence of magnetic anisotropy with the metal–ligand distance (r) and ligand bite angle (θ), we have performed magneto-structural correlations on complex **1** by varying r from 2.56 Å to 2.86 Å and θ from 63° to 83°. We have used the MD-II set up as it reproduces the experimental observables. The correlation denotes that (Fig. 11 and Tables S13–S22†) the ligand bite angle is playing an essential role in dictating the magnetic anisotropy of the uranium centre rather than the U–C bond distance. The energy splitting of the ground and first excited KDs increases with increasing r, but the overall energy splitting of the KDs remains almost constant (Fig. 12a). A close look at Tables S14–S18† reveals that the transverse component of anisotropy increases with increasing r, although the variation is found to be very small. The decrease in transverse anisotropy can be rationalized in terms of computed CASSCF charge (Loprop charge as implemented in MOLCAS) analysis which reveals that the charges of uranium decrease with increasing r value (Fig. 13).

The magnetic anisotropy of the uranium centre is strongly correlated with the C–U–C angle. The variation of θ from the original angle of 73° increases the overall energy splitting of the KDs (Fig. 12b) and decreases the transverse component of anisotropy (Tables S19–S23 in the ESI†). But the energy difference between the ground and first excited KDs increases with increasing θ. The $g_z \gg g_x/g_y$ with increasing θ implies enhancement of axiality with an increase in the ligand bite angle. The
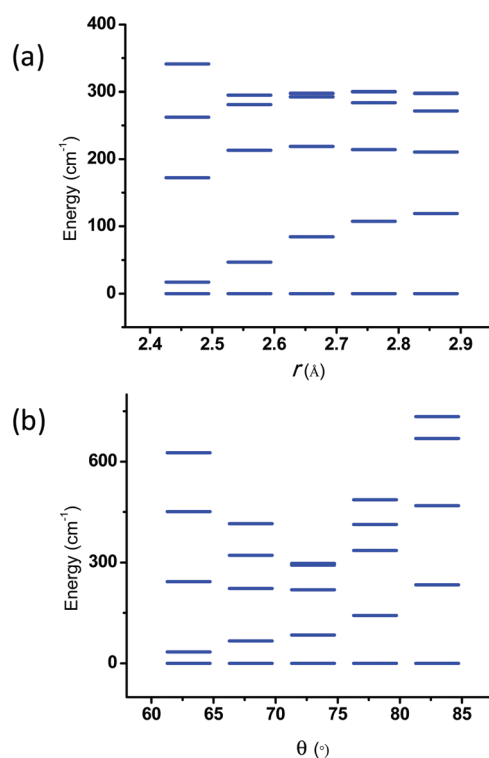
Fig. 12 (a) Energy splitting of the KDs with varying U–C distance. (b) Energy splitting of the KDs with the ligand bite angle (C–U–C).
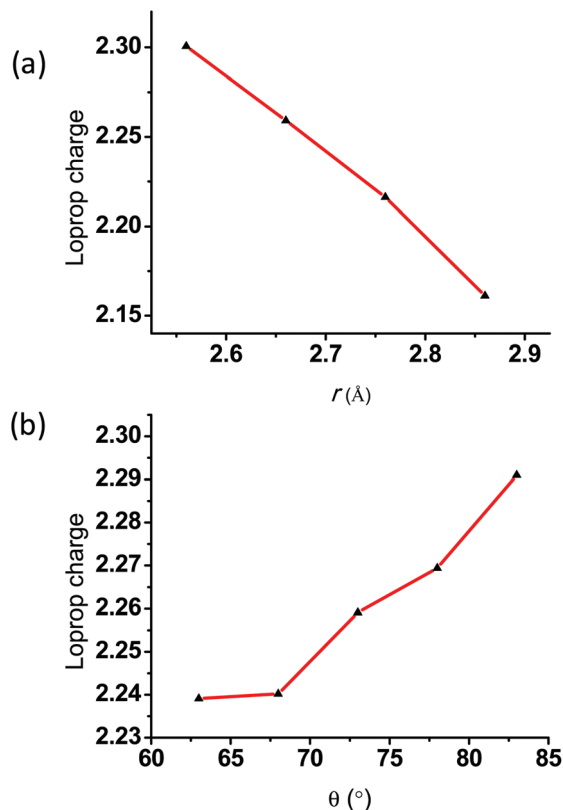
Fig. 13 (a) Computed Loprop charge of the uranium centre with (a) uranium−carbon bond distance (r) and (b) Ligand bite angle (θ).

axiality also increases with decreasing θ, but the enhancement is comparatively small with the former. A CShM analysis of the geometry reveals that the deviation from ideal trigonal prism geometry (C_{3h}) becomes lower with increasing θ value (Table S24 in the ESI†). This correlates well with the findings that the axiality of the molecule increases with large θ values. The increases in the energy splitting can also be rationalised using Loprop charge on the uranium centre where larger θ yields larger charges (Fig. 13b).

4.   Conclusions

Strong dependency of magnetic anisotropy on the U(III) centre by the nature of the coordinating atom of the ligand (carbon *vs.* nitrogen) is studied using *ab initio* calculations employing well-characterised systems [U(BcMe)₃] and [U(BpMe)₃]. Here [U(BcMe)₃] is axially compact compared to [U(BpMe)₃] and this is favourable for oblate uranium(III) ions from an electrostatic point of view. Our calculations show that if a reference of CAS (3,7) is employed where only the 5f electrons in the 5f orbital is considered, both molecules yield very similar magnetic properties exhibiting large QTM and transverse anisotropy in the ground state. However, this is not in agreement with the experimental results where the magnetic properties of [U(BcMe)₃] are superior compared to those of [U(BpMe)₃]. The

additional QTM probability in [U(BpMe)₃] due to the coordinating nitrogen atom suggests that the hyperfine values are reasonably large and could offer a reason for worsening SMM characteristics in [U(BpMe)₃]. However, the field induced SIM behaviour in [U(BcMe)₃] is puzzling and could not be reproduced using this minimal CAS reference space. This is an indispensable point as in lanthanides minimal CAS reference space of incorporating 4f electrons in 4f orbitals reproduces most of the quantifiable experimental observables. Our study suggests that the same cannot be extended for actinide chemistry.

Particularly inclusion of formally empty $6d_{z^2}$ orbitals of uranium found to influence the magnetic properties significantly with the computed results using this set up reproduces all the experimental data (susceptibility, g-factors, ground state m_J level and energy gap between the ground and first excited states). A closer inspection of this orbital reveals a significant contribution of this orbital to the agostic interaction with the –BH₂ group of the ligand, explaining the importance of agostic interactions in controlling the magnetic anisotropy of the U magnets. In trigonal prismatic geometry, the $6d_{z^2}$ orbital is close lying in energy to the 5f orbitals, and therefore its inclusion in the active space is mandatory to reproduce the experimental observables.

The CASPT2 calculations do not improve magnetic susceptibility and the blocking barrier compared to CASSCF calculations. The magneto-structural correlations reveal that the larger bite angle reduces the QTM and enhances the SIM characteristics. The metal–ligand covalency has been enhanced by *in silico* design of a model complex where carbon donor atoms of [U(BcMe)₃] have been replaced by sulphur. This model is found to have superior SIM characteristics compared to its other congeners. The QTAIM analysis clearly explains the nature of coordination and the reason for the anisotropy direction. Quite interestingly, the highly curved bond paths at the H–BH₂, higher ellipticity (ε), smaller $\rho(r)$ and positive $\nabla^2_{\rho(r)}$ values confirm the presence of agostic interactions between the uranium and H–BH₂ offering experimental chemists an additional way to fine tune the magnetic anisotropy in uranium SIMs.

Conflicts of interest

There are no conflicts to declare.

Acknowledgements

References

1 N. Ishikawa, M. Sugita, T. Okubo, N. Tanaka, T. Iino and Y. Kaizu, *Inorg. Chem.*, 2003, **42**, 2440–2446.

2 J. D. Rinehart and J. R. Long, *Chem. Sci.*, 2011, **2**, 2078.

3 C. A. Gaggioli and L. Gagliardi, *Inorg. Chem.*, 2018, **57**, 8098–8105.

4 S. G. McAdams, A.-M. Ariciu, A. K. Kostopoulos, J. P. Walsh and F. Tuna, *Coord. Chem. Rev.*, 2017, **346**, 216–239.

5 J. D. Rinehart and J. R. Long, *Dalton Trans.*, 2012, **41**, 13572–13574.

6 J. J. Le Roy, S. I. Gorelsky, I. Korobkov and M. Murugesu, *Organometallics*, 2015, **34**, 1415–1418.

7 C. A. Gaggioli and L. Gagliardi, *Inorg. Chem.*, 2018, **57**(14), 8098–8105.

8 K. R. Meihaus, S. G. Minasian, W. W. Lukens Jr., S. A. Kozimor, D. K. Shuh, T. Tyliszczak and J. R. Long, *J. Am. Chem. Soc.*, 2014, **136**, 6056–6068.

9 M. Spivak, K. D. Vogiatzis, C. J. Cramer, C. d. Graaf and L. Gagliardi, *J. Phys. Chem. A*, 2017, **121**, 1726–1733.

10 F. Cortés-Guzmán and R. F. Bader, *Coord. Chem. Rev.*, 2005, **249**, 633–662.

11 P. S. V. Kumar, V. Raghavendra and V. Subramanian, *J. Chem. Sci.*, 2016, **128**, 1527–1536.

12 F. Aquilante, J. Autschbach, R. K. Carlson, L. F. Chibotaru, M. G. Delcey, L. De Vico, I. F. Galván, N. Ferré, L. M. Frutos and L. Gagliardi, *J. Comput. Chem.*, 2016, **37**, 506–541.

13 Y.-C. Chen, J.-L. Liu, L. Ungur, J. Liu, Q.-W. Li, L.-F. Wang, Z.-P. Ni, L. F. Chibotaru, X.-M. Chen and M.-L. Tong, *J. Am. Chem. Soc.*, 2016, **138**, 2829–2837.

14 B. O. Roos, V. Veryazov and P.-O. Widmark, *Theor. Chem. Acc.*, 2004, **111**, 345–351.

15 A. Wolf, M. Reiher and B. A. Hess, *J. Chem. Phys.*, 2002, **117**, 9215–9226.

16 F. Aquilante, P.-Å. Malmqvist, T. B. Pedersen, A. Ghosh and B. O. Roos, *J. Chem. Theory Comput.*, 2008, **4**, 694–702.

17 P. Å. Malmqvist, B. O. Roos and B. Schimmelpfennig, *Chem. Phys. Lett.*, 2002, **357**, 230–240.

18 J. Finley, P.-Å. Malmqvist, B. O. Roos and L. Serrano-Andrés, *Chem. Phys. Lett.*, 1998, **288**, 299–306.

19 L. F. Chibotaru, L. Ungur and A. Soncini, *Angew. Chem., Int. Ed. Engl.*, 2008, **47**, 4126–4129.

20 L. Ungur, M. Thewissen, J.-P. Costes, W. Wernsdorfer and L. F. Chibotaru, *Inorg. Chem.*, 2013, **52**, 6328–6337.

21 L. F. Chibotaru, L. Ungur, C. Aronica, H. Elmoll, G. Pilet and D. Luneau, *J. Am. Chem. Soc.*, 2008, **130**, 12445–12455.

22 W. Küchle, M. Dolg, H. Stoll and H. Preuss, *J. Chem. Phys.*, 1994, **100**, 7535–7542.

23 X. Cao and M. Dolg, *J. Mol. Struct.*, 2004, **673**, 203–209.

24 A. D. Becke, *J. Chem. Phys.*, 1993, **98**, 5648–5652.

25 A. Schäfer, H. Horn and R. Ahlrichs, *J. Chem. Phys.*, 1992, **97**, 2571–2577.

26 A. Schäfer, C. Huber and R. Ahlrichs, *J. Chem. Phys.*, 1994, **100**, 5829–5835.

27 D. Andrae, U. Haeussermann, M. Dolg, H. Stoll and H. Preuss, *Theor. Chem. Acc.*, 1990, **77**, 123–141.

28 M. J. Frisch, G. W. Trucks, H. B. Schlegel, G. E. Scuseria, M. A. Robb, J. R. Cheeseman, G. Scalmani, V. Barone, B. Mennucci, G. A. Petersson, H. Nakatsuji, M. Caricato, X. Li, H. P. Hratchian, A. F. Izmaylov, J. Bloino, G. Zheng, J. L. Sonnenberg, M. Hada, M. Ehara, K. Toyota, R. Fukuda, J. Hasegawa, M. Ishida, T. Nakajima, Y. Honda, O. Kitao, H. Nakai, T. Vreven, J. A. Montgomery Jr., J. E. Peralta, F. Ogliaro, M. J. Bearpark, J. Heyd, E. N. Brothers, K. N. Kudin, V. N. Staroverov, R. Kobayashi, J. Normand, K. Raghavachari, A. P. Rendell, J. C. Burant, S. S. Iyengar, J. Tomasi, M. Cossi, N. Rega, N. J. Millam, M. Klene, J. E. Knox, J. B. Cross, V. Bakken, C. Adamo, J. Jaramillo, R. Gomperts, R. E. Stratmann, O. Yazyev, A. J. Austin, R. Cammi, C. Pomelli, J. W. Ochterski, R. L. Martin, K. Morokuma, V. G. Zakrzewski, G. A. Voth, P. Salvador, J. J. Dannenberg, S. Dapprich, A. D. Daniels, Ö. Farkas, J. B. Foresman, J. V. Ortiz, J. Cioslowski and D. J. Fox, *Gaussian 09, Revision A.02*, Gaussian, Inc., Wallingford, CT, USA, 2009.

29 F. Biegler-König and J. Schönbohm, *J. Comput. Chem.*, 2002, **23**, 1489–1494.

30 D. Maganas, S. Sottini, P. Kyritsis, E. J. Groenen and F. Neese, *Inorg. Chem.*, 2011, **50**, 8741–8754.

31 M. Llunell, D. Casanoval, J. Cirera, P. Alemany and S. Alvarez, *SHAPE, v2. 1*, University of Barcelona and The Hebrew University of Jerusalem, Barcelona and Jersalem, 2013.

32 T. Gupta, G. Velmurugan, T. Rajeshkumar and G. Rajaraman, *J. Chem. Sci.*, 2016, **128**, 1615–1630.

33 V. Tognetti, L. Joubert, R. Raucoules, T. De Bruin and C. Adamo, *J. Phys. Chem. A*, 2012, **116**, 5472–5479.

34 P. Popelier and G. Logothetis, *J. Organomet. Chem.*, 1998, **555**, 101–111.

35 I. F. Díaz-Ortega, J. M. Herrera, D. Aravena, E. Ruiz, T. Gupta, G. Rajaraman, H. Nojiri and E. Colacio, *Inorg. Chem.*, 2018, **57**, 6362–6375.

36 S. T. Liddle and J. van Slageren, *Chem. Soc. Rev.*, 2015, **44**, 6655–6669.

37 J. T. Coutinho, M. A. Antunes, L. C. Pereira, H. Bolvin, J. Marcalo, M. Mazzanti and M. Almeida, *Dalton Trans.*, 2012, **41**, 13568–13571.

38 R. Layfield, F. S. Guo, A. Mansikkamaki, M. L. Tong and Y. C. Chen, *Angew. Chem., Int. Ed. Engl.*, 2019, DOI: 10.1002/anie.201903681.

39 M. Autillo, L. Guerin, H. Bolvin, P. Moisy and C. Berthon, *Phys. Chem. Chem. Phys.*, 2016, **18**, 6515–6525.

40 M. A. Antunes, I. C. Santos, H. Bolvin, L. C. Pereira, M. Mazzanti, J. Marcalo and M. Almeida, *Dalton Trans.*, 2013, **42**, 8861–8867.

41 R. Alessandri, H. Zulfikri, J. Autschbach and H. Bolvin, *Chem. – Eur. J.*, 2018, **24**, 5538–5550.

42 J. Jung, M. Atanasov and F. Neese, *Inorg. Chem.*, 2017, **56**, 8802–8816.

43 B. Scheibe, C. Pietzonka, O. Mustonen, M. Karppinen, A. J. Karttunen, M. Atanasov, F. Neese, M. Conrad and F. Kraus, *Angew. Chem.*, 2018, **130**, 2964–2968.

44 S. K. Singh, M. F. Beg and G. Rajaraman, *Chem. – Eur. J.*, 2016, **22**, 672–680.

45 M. M. Hänninen, A. J. Mota, R. Sillanpää, S. Dey, G. Velmurugan, G. Rajaraman and E. Colacio, *Inorg. Chem.*, 2018, **57**, 3683–3698.

46 S. K. Singh, N. K. Tibrewal and G. Rajaraman, *Dalton Trans.*, 2011, **40**, 10897–10906.

47 G. Rajaraman, F. Totti, A. Bencini, A. Caneschi, R. Sessoli and D. Gatteschi, *Dalton Trans.*, 2009, 3153–3161.

48 T. Rajeshkumar, S. K. Singh and G. Rajaraman, *Polyhedron*, 2013, **52**, 1299–1305.

49 S. K. Singh, T. Gupta, L. Ungur and G. Rajaraman, *Chem. – Eur. J.*, 2015, **21**, 13812–13819.

50 M. E. Boulon, G. Cucinotta, J. Luzon, C. Degl'Innocenti, M. Perfetti, K. Bernot, G. Calvez, A. Caneschi and R. Sessoli, *Angew. Chem., Int. Ed.*, 2013, **52**, 350–354.

51 G. Cucinotta, M. Perfetti, J. Luzon, M. Etienne, P. E. Car, A. Caneschi, G. Calvez, K. Bernot and R. Sessoli, *Angew. Chem., Int. Ed.*, 2012, **51**, 1606–1610.

52 G. Feng, M. Zhang, D. Shao, X. Wang, S. Wang, L. Maron and C. Zhu, *Nat. Chem.*, 2019, **11**, 248.

53 T. Arliguie, C. Lescop, L. Ventelon, P. C. Leverd, P. Thuéry, M. Nierlich and M. Ephritikhine, *Organometallics*, 2001, **20**, 3698–3703.

54 L. Maria, Â. Domingos and I. Santos, *Inorg. Chem.*, 2001, **40**, 6863–6864.

55 W. Clegg, O. Glemser, K. Harms, G. Hartmann, R. Mews, M. Noltemeyer and G. Sheldrick, *Acta Crystallogr.*, 1981, **37**, 548–552.

56 F. H. Allen, O. Kennard, D. G. Watson, L. Brammer, A. G. Orpen and R. Taylor, *J. Chem. Soc., Perkin Trans. 2*, 1987, S1–S19.